Proceedings of the Thirteenth International Conference on
Engineering Computational Technology
Edited by: P. Iványi, J. Kruis and B.H.V. Topping
Civil-Comp Conferences, Volume 13, Paper 2.2
Civil-Comp Press, Edinburgh, United Kingdom, 2026
ISSN: 2753-3239, doi: 10.4203/ccc.13.2.2

Adaptive Lattice Boltzmann Large Eddy Simulation of Turbulent Flows Through Porous Structures with Improved Mesh Interface Treatment

D. Kashyap[1], M. Grondeau[2] and R. Deiterding[1]

[1] Aeronautics & Astronautics, University of Southampton, United Kingdom
[2] Laboratoire Universitaire des Sciences Appliquées, Université de Caen, Cherbourg , France

Abstract

Turbulent flows interacting with porous media are prevalent in many engineering and environmental applications, but understanding how turbulence interacts with porous materials under varied conditions remains a critical research problem. This paper evaluates a large-eddy simulation framework for turbulent flow through porous structures and demonstrates it for regular square-bar arrays, with Reynolds numbers up to $Re = 40000$. The methodology captures critical flow properties such as interfacial shear layers and pore-scale vortical structures by combining adaptive mesh refinement with a lattice Boltzmann solver (AMROC-LBM). Adaptive refinement focuses on dynamically active regions, particularly those near the porous-fluid interface, which exhibit high gradients and turbulence. This method incurs lower computational costs than a uniformly fine grid. The non-equilibrium distribution rescaling approach, according to the systematic evaluation of interface treatment strategies, guarantees robust and physically consistent information flow across grid levels.

Keywords: turbulent flow, porous medium, large eddy simulation, lattice Boltzmann method, dynamic mesh adaptation, parallel computing

1 Introduction

Understanding and improving a variety of natural and artificial processes, including as filtration, stream-groundwater interactions, packed-bed reactors, gas drying technologies, and heat exchangers, depends on the interaction between turbulent flow and porous media [1]. In recent decades, many research initiatives have focused on linking empirical models, interface theories, and detailed pore-scale simulations to illuminate the intricate and often subtle physics that arises at fluid-porous interfaces. Improvements in computational power have facilitated direct numerical simulations (DNS) [2–4] and large-eddy simulations (LES) [5–7] that capture turbulent structures over porous media made up of packed cylinders or more intricate matrix geometries. In this framework, the lattice Boltzmann method (LBM) [8, 9] has emerged as a particularly appealing technique since its mesoscopic formulation easily accommodates complex configurations.

The lattice Boltzmann method (LBM) community generally studies porous media flows using two main approaches. One is a pore-scale simulation in which the fluid-structure interaction is resolved directly. The other is representative elementary volume (REV) modelling, which relies on spatial averaging to reduce computational cost. Although REV approaches are attractive for large domains, they cannot capture the detailed flow physics at the pore level. The mesoscopic nature of LBM offers a useful balance, resolving pore-scale dynamics while remaining computationally manageable. However, most existing simulations still consider idealised flow configurations in which porous media fill the entire channel length, allowing the use of fully periodic boundary conditions, as in the comprehensive DNS studies by Kuwata *et al.* [4]. In addition, the LBM community focuses mainly on stabilising the method across a wide range of applications while introducing multiple collision models, including two-relaxation-time (TRT), multiple-relaxation-time (MRT), and projection-based (PR) LBM [10]. However, being regarded as a relatively low-dissipative numerical approach in incompressible flow regimes, LBM is well-suited for large-eddy simulations of turbulent flows. The present study demonstrates pore-scale LBM simulations of fluid flow and turbulence within porous media while building on the original LBM-LES formulation of Hou *et al.* [11], with several important developments. The method offers computational scalability through advanced algorithms such as adaptive mesh refinement and BGK-based recursive regularised collision operators. Compared with DNS-LBM approaches, the present framework achieves substantially improved computational efficiency while maintaining high solution fidelity [12]. The robustness of the present method is supported by three main elements: (1) dynamic SAMR, which significantly reduces the total cell count compared with uniform meshes, (2) a recursive regularised single-relaxation-time collision operator [13] that enhances numerical stability at high Reynolds numbers, and (3) an MPI-parallel implementation

suitable for large-scale simulations.

The paper is organised as follows: Section 2 describes the adaptive LBM-LES framework implemented in AMROC-LBM. Section 3 presents validation studies. Section 4 reports results in detail. Section 5 sums up the main findings.

2 Adaptive lattice Boltzmann solver

The LBM was developed from lattice gas automata and tracks the evolution of a particle distribution function (PDF), the only unknown quantity in the LBM, to represent fluid flow using the discrete Boltzmann equation. By calculating the hydrodynamic moments of the distribution function $f(\mathbf{x}, \xi, t)$, LBM mainly concentrates on averaging macroscopic variables, such as density and velocity.

2.1 Lattice Boltzmann method

The LBM approach uses discrete space $\mathbf{x}$, time t, and velocity ξ to solve the kinetic equation of the discrete PDF, making it a special finite-difference scheme. The lattice structure in LBM is represented by the symbol DmQn, where m is the number of dimensions and n is the number of particle velocities. The D3Q27 model, which uses 27 unit direction vectors $\mathbf{e}_\alpha$, is used for all three-dimensional computations herein.

It is standard to implement LBM internally on a non-dimensional unit lattice. The LBM algorithm begins by setting the initial values of the distribution functions using the discrete equilibrium distribution function generated from non-dimensionalised required macroscopic variables. The two main stages of the algorithm are streaming and collision [9]. The streaming step models the movement of the distribution function from one node to the next in the direction of motion, as follows

$$\check{f}_\alpha(\mathbf{x}, t) = f_\alpha(\mathbf{x} - \mathbf{e}_\alpha, t). \tag{1}$$

The collision step employs a regularised Bhatnagar-Gross-Krook (BGK) collision operator [13], incorporating a forcing term F_α.

$$f_\alpha(\mathbf{x}, t + \Delta t) = \check{f}_\alpha^{(0)}(\mathbf{x}, t) + (1 - \omega)\check{f}_\alpha^{(1)}(\mathbf{x}, t) + F_\alpha(\mathbf{x}, t). \tag{2}$$

The dimensionless relaxation frequency ω defines the kinematic viscosity of the fluid according to the following relationship:

$$\nu = c_s^2 \left(\frac{1}{\omega} - \frac{1}{2} \right) \Delta t. \tag{3}$$

The speed of sound is set here to $c_s = 340\,\mathrm{m/s}$ and remains constant throughout all simulations, while Δt denotes the physical time step. In Eq. (2), the $\check{}$ superscript indicates the post-propagation state. The equilibrium $f_\alpha^{(0)}$ and non-equilibrium $f_\alpha^{(1)} = f_\alpha - f_\alpha^{(0)}$ components are computed using the recursive regularised (RR) formulation

proposed by Malaspinas [13]. Our implementation employs the recursive approach up to order 6 for both equilibrium and non-equilibrium parts. It has been established among the research community that this RR-BGK scheme is stable and accurate at high Reynolds numbers.

To convert non-dimensional lattice distributions to physical values, suitable scaling is needed depending on the physical time step Δt and physical grid spacing Δx of the Cartesian mesh, using the lattice speed $c = \Delta x/\Delta t$. In LBM, moments of the distribution function provide the macroscopic variables. For example, rescaling the 0^{th} and 1^{st} moments of the PDF by the reference density ρ_0 and the lattice speed, respectively, yields the gas density ρ and velocity vector $\mathbf{u}$ as follows:

$$\rho = \rho_0 \sum_{\alpha} f_\alpha, \qquad \mathbf{u} = c \sum_{\alpha} \mathbf{e}_\alpha f_\alpha. \tag{4}$$

The density can be used to calculate total pressure as $p = c_s^2(\rho - \rho_0) + p_0$, where $c_s = c\tilde{c}_s$ is the speed of sound and p_0 is the ambient pressure. For D3Q27, the lattice speed of sound $\tilde{c}_s$ is $1/\sqrt{3}$.

2.2 Interface treatment in adaptive mesh refinement

In LBM, the necessary requirement is that the relaxation frequency in Eq. (3) remains below 2 to avoid numerical instability, which imposes a lower bound on the kinematic viscosity. Consequently, simulations of low viscosity (high Reynolds number) flows require lattice refinement, which becomes prohibitively expensive on uniform grids. To mitigate this cost, a block-structured adaptive mesh refinement (SAMR) strategy with accurate grid-interface treatment is employed, which is particularly important for LBM where information propagates locally via particle distribution functions. The present solver uses a uniform Cartesian discretisation combined with SAMR in the AMROC framework [14, 15]. In this approach, computational cells are clustered into non-overlapping rectangular grids by a dedicated clustering algorithm. Each grid is equipped with halo (ghost) cells that enable enforcement of physical boundary conditions and inter-level synchronisation. At coarse–fine interfaces, specialised treatment is required to ensure consistent transport of distribution functions and conservation of macroscopic quantities. Two complementary interface strategies are considered: (i) an explode-coalesce AMR technique [16] implemented in a recursive correction procedure, and (ii) a rescaling approach following Dupuis and Chopard [17] to improve consistency of the non-equilibrium distribution function contribution.

2.2.1 Explode-Coalesce AMR technique

The first strategy follows the block-structured AMR method of Berger and Colella [18], originally developed for explicit finite-volume schemes for hyperbolic conservation laws. For two adjacent refinement levels, the spatial and temporal resolutions

satisfy

$$\frac{\Delta x^c}{\Delta x^f} = \frac{\Delta t^c}{\Delta t^f} = r, \tag{5}$$

where superscripts c and f denote coarse and fine levels, respectively, and $r \geq 2$ is the refinement ratio. The simultaneous refinement of space and time is consistent with the explicit nature of the LBM. A cell-centred formulation is adopted so that the LBM integrates naturally into the recursive AMR hierarchy of AMROC [14], which makes the scheme also conservative in ρ and $\mathbf{u}$.

In adaptive LBM, the relaxation frequency must be adjusted on each level according to Eq. (3). Distinguishing between the transport and collision operators, $\mathcal{T}$ and $\mathcal{C}$, the interface procedure for a refinement ratio $r = 2$ proceeds as follows:

1. Complete update on the coarse grid:

$$f_\alpha^{C,n+1} = \mathcal{C}\mathcal{T}\left(f_\alpha^{C,n}\right). \tag{6}$$

2. Construct fine-grid halo values $f_{i,\text{in}}^{F,n}$ from the subset of coarse distributions $f_{i,\text{in}}^{C,n}$ that propagate into the refined region.

3. Perform transport on the fine grid,

$$\tilde{f}_\alpha^{F,n} = \mathcal{T}\left(f_\alpha^{F,n}\right), \tag{7}$$

   and apply collision only in interior fine cells to obtain $f_\alpha^{F,n+1/2}$.

4. Repeat the fine-level transport–collision step to advance the fine grid to time level $n + 1$.

5. Average outgoing fine-grid halo distributions to obtain interface values.

$$\tilde{f}_{\alpha,\text{out}}^{C,n}. \tag{8}$$

6. Apply inverse transport,

$$\bar{f}_{\alpha,\text{out}}^{C,n} = \mathcal{T}^{-1}\left(\tilde{f}_{\alpha,\text{out}}^{C,n}\right), \tag{9}$$

   and overwrite the corresponding pre-streaming coarse-grid values.

7. Parallel Synchronisation of the corrected coarse-level distributions.

8. Recompute the update for coarse cells adjacent to the refinement boundary using the corrected interface data.

This algorithm is computationally equivalent to the method proposed by Chen *et al.* [16] but conforms to the Berger-Colella recursion, in which coarse levels are advanced first and subsequently corrected. Because the collision operator is non-linear, coarse cells sharing faces or corners with refined regions must be recomputed to maintain consistency.

2.2.2 Non-equilibrium distribution rescaling approach

An alternative coupling strategy is based on the theoretical framework of Dupuis and Chopard [17]. In this approach, equilibrium and non-equilibrium parts of the distribution functions are treated separately during inter-level transfer. Fine-to-coarse transfer is performed via averaging, while coarse-to-fine transfer uses spatial and temporal interpolation.

The non-equilibrium components are rescaled according to

$$f_\alpha^c = f_\alpha^{(0),f\to c} + \frac{r\omega^f}{\omega^c} f_\alpha^{(1),f\to c}, \tag{10}$$

$$f_\alpha^f = f_\alpha^{(0),c\to f} + \frac{\omega^c}{r\omega^f} f_\alpha^{(1),c\to f}, \tag{11}$$

where ω^c and ω^f denote the relaxation frequencies on the coarse and fine levels. This formulation preserves continuity of density and velocity while maintaining consistency of the strain-rate tensor through appropriate scaling of the non-equilibrium component.

2.3 Large eddy simulation models

To enable turbulent flow simulations at high Reynolds numbers, unresolved scales are modelled using large eddy simulation (LES). The Smagorinsky model [19] is employed, introducing an eddy viscosity

$$\nu_t = (C_{sm}\Delta x)^2 |\overline{S}|, \tag{12}$$

where C_{sm} is the Smagorinsky constant, Δx is the grid spacing, and the characteristic filtered strain rate is defined as $|\overline{S}| = \sqrt{2\overline{S}_{ij}\overline{S}_{ij}}$ which is computed using the consistent formulation of Malaspinas [20] in the present work.

The subgrid-scale contribution to the relaxation time is calculated as $\tau_{sgs} = \nu_t/c_s^2$. The total kinematic viscosity thus becomes $\nu+\nu_t$, yielding an effective relaxation time of $\tau_{\mathit{eff}} = \tau + \tau_{sgs}$. The modified relaxation frequency, $\omega^\star = 1/\tau_{\mathit{eff}}$, is consequently expressed as

$$\omega^\star = \frac{c_s^2\Delta t}{(\nu+\nu_t) + \frac{1}{2}c_s^2\Delta t}. \tag{13}$$

3 Test problem for validation

For validation purposes, the porous-flow setup of Suga et al. [21] is adopted, which is simulated under isothermal conditions, with adiabatic side walls. This configuration consists of flow through a rectangular duct partially filled with a porous medium composed of rectangular bars, occupying half of the channel height. A bulk velocity of 10 m/s is imposed, corresponding to $Re = 7400$.

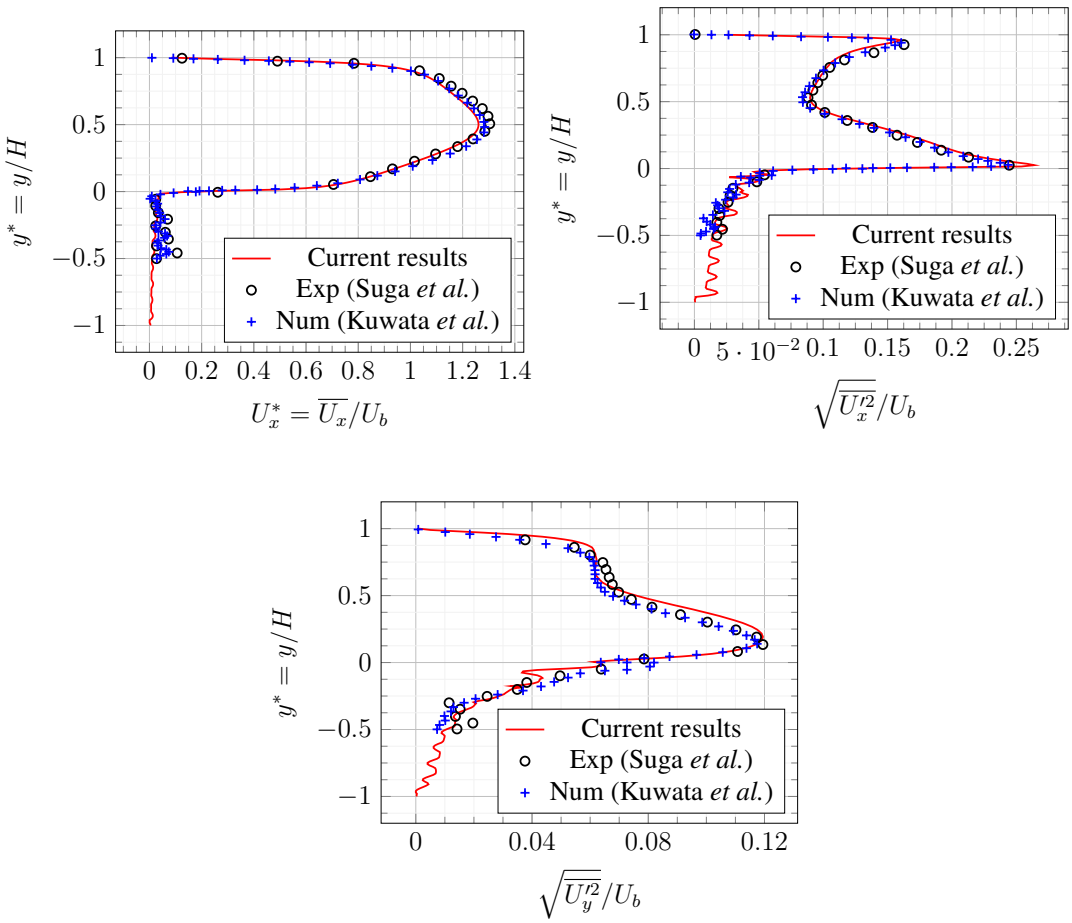

Figure 1: Comparison of time and spatial averaged velocity profile (top left), streamwise normal stress ($\overline{U_x'^2}$, top right) and vertical normal stress ($\overline{U_y'^2}$, bottom) with Suga *et al.*'s numerical and experimental results.

A quantitative assessment of the turbulence statistics is presented in Figure 1, comparing the current results with experimental data from Suga *et al.* [21] and numerical data from Kuwata *et al.* [4] for $Re_H = 7400$. The comparison includes span-averaged profiles of temporal mean velocity and Reynolds stresses. The simulation shows satisfactory agreement with the experimental data in the clear-fluid region. However, the observed discrepancies are attributed to the current computational model's simplification of neglecting conjugate heat transfer effects, particularly within the porous region, where thermal effects are most pronounced.

4 Results and discussion

This section investigates the development of turbulent flow in a channel containing a centrally placed porous structure, corresponding to configurations used in an ongoing collaborative experimental study. The flow configuration (Figure 2a) consists

of a channel flow through a porous block formed by a regular array of square bars of size $D = 0.0127$ m. The domain dimensions are $L_x = 16.7H$, $L_y = 4H$, and $L_z = 2H$, where $H = 0.0762$ m denotes the characteristic height of the porous block. The porous section extends 0.613 m in the streamwise direction and is positioned $2H$ downstream of the inlet. This arrangement yields a porosity of $\phi = 0.48$. A uniform inlet velocity profile with $U_{in} = 8$ m/s is prescribed, corresponding to a Reynolds number based on the block height of $Re_H = 40000$.

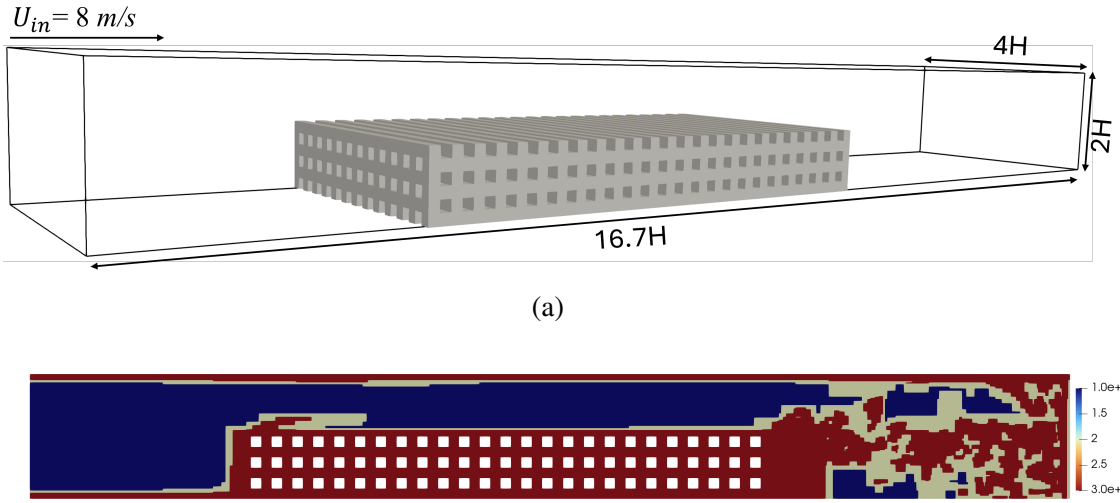

(a)

(b)

Figure 2: (a) Schematic of the computational domain showing the porous block composed of square bars (b) AMR levels

4.1 Comparison of interface treatment

Figure 3 compares the performance of the two different grid refinement interface techniques for the present porous block with streamwise periodicity while imposing streamwise driving force to sustain a fully developed turbulent state. The results are presented as the velocity vector magnitude in the X-Z plane. The explode-coalesce method (cf. Figures 3(a,c)), produces significant non-physical artifacts at the interface boundary, which is also evident from the plots of spatially and temporally averaged streamwise velocity U_x/U_b and streamwise turbulence intensity $\sqrt{R_{11}}/U_b$ (where, $R_{11} = \overline{U_x'^2}$) across the channel height (cf. Figure 4). However, the non-equilibrium distribution rescaling approach (cf. Figure 3(b,d)) produces a high-fidelity solution, as evidenced by a cleaner flow field at the refined levels. The correlation between velocity overshoot and elevated Reynolds stress shows that the explode-coalesce method fails to ensure consistent transfer of momentum and higher-order moments across the refinement interface. This inconsistency causes numerical imbalance, leading to unphysical amplification of turbulent intensity at the interface. All subsequent simulations have hence used the non-equilibrium rescaling approach.

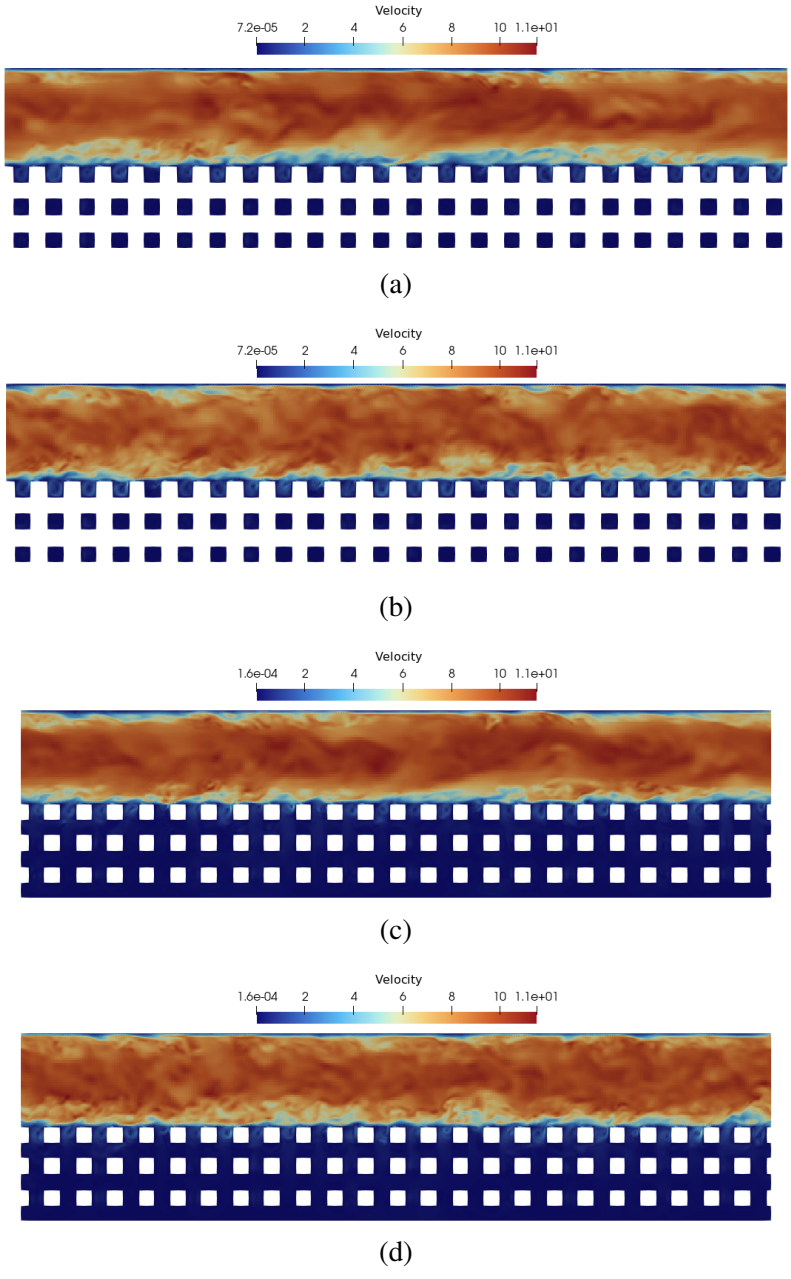

Figure 3: Comparison of two interface methods with streamwise velocity magnitude at crest and trough plane respectively (a,c) Explode-coalesce method and (b,d) Non-equilibrium distribution rescaling approach

4.2 Analysis of present flow configuration

Figure 5 offers additional insight into this mechanism by presenting instantaneous contours of velocity and vorticity vectors magnitudes at crest and trough planes for

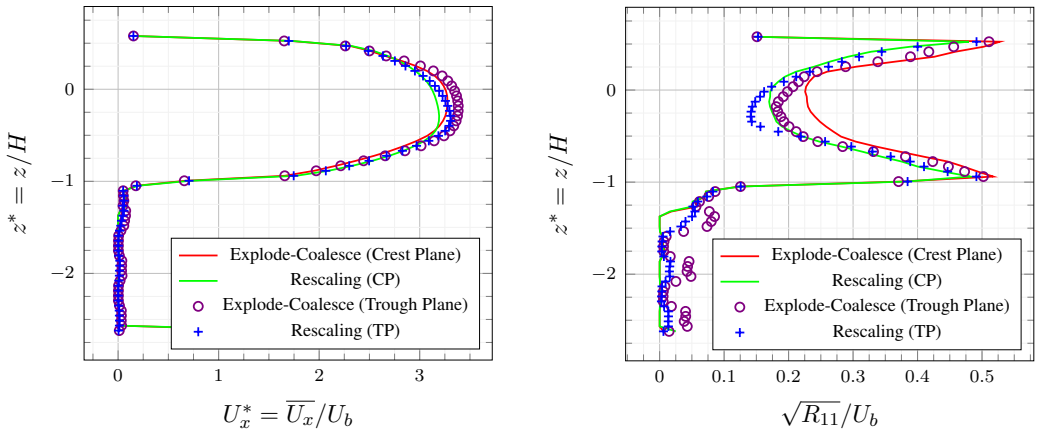

Figure 4: Comparison of interface treatment in terms of time and spatial averaged velocity profile (left), streamwise normal Reynolds stress (right).

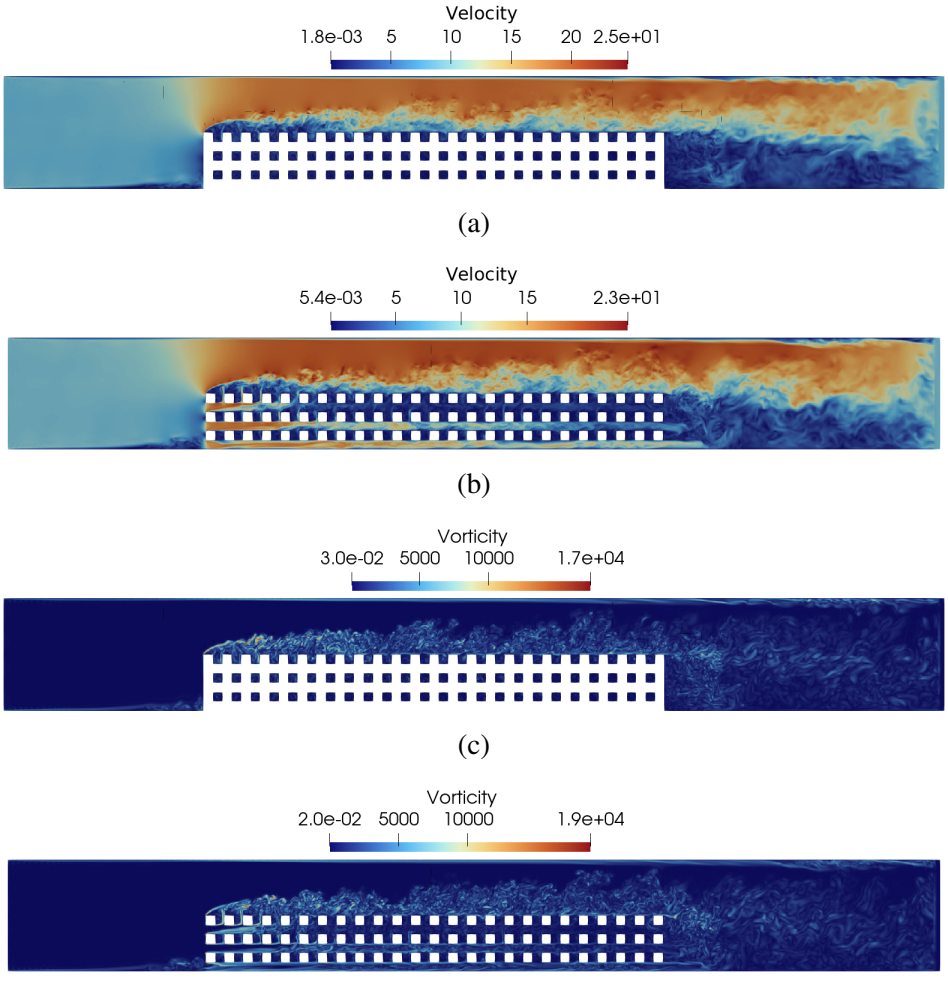

Figure 5: Contours of (a,b) velocity vector magnitude and (c,d) vorticity vector magnitude at crest and trough planes, respectively.

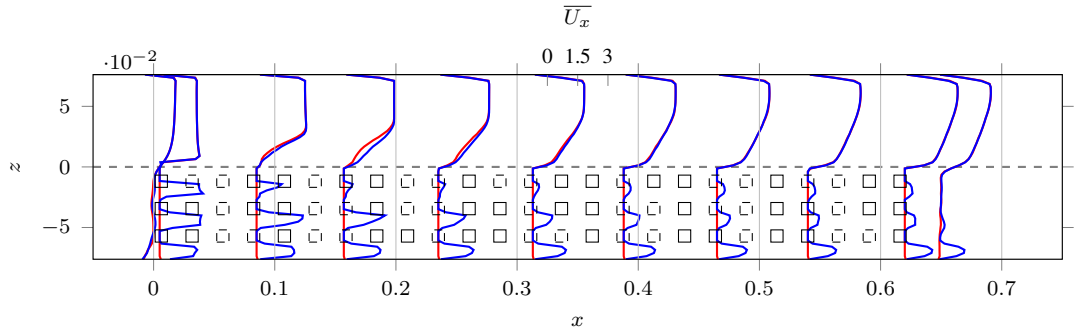

Figure 6: Time averaged streamwise velocity profiles at their respective x locations through crest (red) and trough (blue) planes respectively.

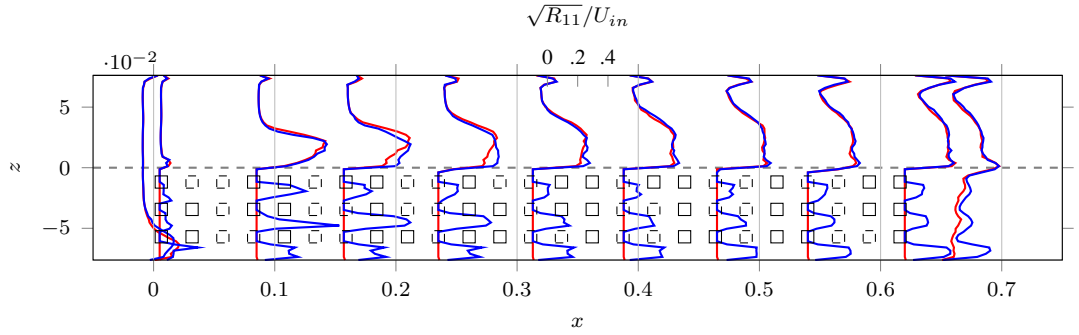

Figure 7: Time averaged streamwise normal Reynolds stress profiles at their respective x locations through crest (red) and trough (blue) planes respectively.

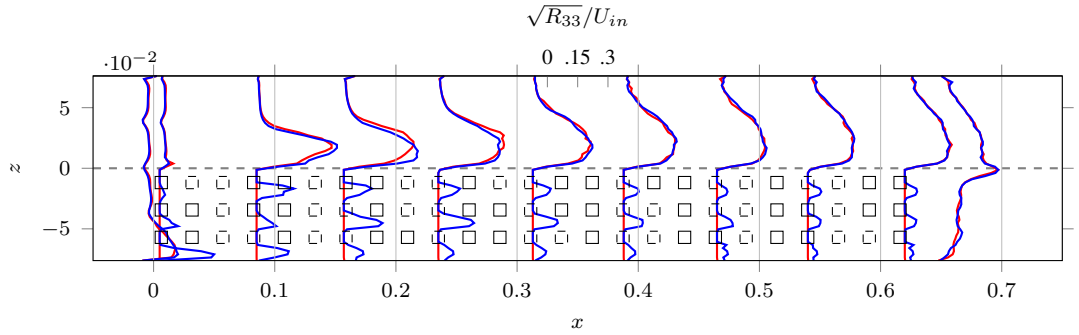

Figure 8: Time averaged vertical normal Reynolds stresses at their respective x locations through crest (red) and trough (blue) planes respectively.

the square-bar configuration. The velocity field confirms strong stratification between the outer flow and the porous region, while the vorticity contours reveal the local evolution of the shear layer. The distinction between crest and trough planes is most pronounced within the porous region, and it is also evident from the velocity and Reynolds stress profiles, as shown in Figures 6, 7 and 8. The crest plane exhibits

stronger geometric confinement and weaker in-block transport. However, the trough plane permits more direct channelling through the porous structure. Despite these differences, both planes display qualitatively similar downstream wakes, suggesting that large-scale turbulence dynamics are primarily governed by interfacial shear-layer growth and subsequent wake mixing. Collectively, these figures indicate that turbulence generation is initiated at the leading edge by shear-layer instability, while the porous structure strongly influences its subsequent evolution and breakdown.

Figures 6, 7, and 8 show how the time averaged normalised streamwise velocity $\overline{U_x}/U_{in}$, the streamwise normal Reynolds stress $\sqrt{R_{11}}/U_{in}$, and the vertical normal Reynolds stress $\sqrt{R_{33}}/U_{in}$ change with streamwise locations of the flow domain for Reynolds number $Re_H = 40000$. Red lines show profiles taken at the crest plane, while blue lines show those from the trough plane. This highlights the spatial differences in turbulence and momentum transport caused by the porous geometry. When the flow enters the porous structure ($x = 0$ to 0.3), both velocity and Reynolds stress profiles change significantly because of the blockage from the porous bars. The flow speeds up and slows down locally as it moves through the pore spaces. The crest plane usually has larger drops in velocity than the trough plane, which suggests more momentum is lost due to greater obstruction and form drag. Steep velocity gradients near the porous-fluid interface show where interfacial shear layers form. Further downstream, turbulent mixing helps the flow recover, but wake effects can still be seen. The wall-normal stress is lower than $\sqrt{R_{11}}/U_{in}$, which matches the expected turbulence anisotropy in channel flows. Higher stress levels continue downstream, showing that turbulence from the wakes created by the porous structure remains present.

5 Conclusions

The adaptive AMROC-LBM framework and large-eddy simulation make it possible to model turbulent flows in complex porous materials with accuracy and computing efficiency. When compared to a uniform grid, the adaptive mesh refinement method lowers computational costs without sacrificing solution accuracy as it employs finer grids on the regions of interest with turbulence and steep gradients. Validation against established experimental and numerical reference data for a fully developed, streamwise-periodic porous configuration confirms that the method accurately represents the dominant mechanisms of momentum exchange and turbulence generation across the interface. To demonstrate the importance of consistent connection across grid levels for numerical stability and physical accuracy, two distinct interface techniques have been examined. In the present flow configuration, the differences between crest and trough planes highlight the three-dimensional spatial heterogeneity introduced by the porous geometry, particularly within the porous layer where local blockage and pore-scale interactions dominate. The enhanced Reynolds stresses near the porous-fluid interface confirm that this region acts as a turbulence production zone, driven by strong shear and wake interactions. In the future, we will use AMR-based LBM-DNS to thoroughly resolve turbulence, compare the outcomes with upcoming collaborative

experimental data, and expand the existing framework to include heat transfer effects.

Acknowledgement

This work is supported by EPSRC grant number EP/W03350X/1: *Fundamental understanding of turbulent flow over fluid-saturated complex porous media*. Computational resources and support are provided by the ARCHER2 HPC facility. The authors also acknowledge the use of the IRIDIS HPC facility.

References

[1] B. D. Wood, X. He, S. V. Apte, "Modeling Turbulent Flows in Porous Media", Annual Review of Fluid Mechanics, 52, 171–203, 2020, DOI:10.1146/annurev-fluid-010719-060317

[2] Y. Jin, A. Kuznetsov, "Turbulence Modeling for Flows in Wall-Bounded Porous Media: An Analysis Based on Direct Numerical Simulations", Physics of Fluids, 29, 045102, 2017, DOI:10.1063/1.4979062

[3] X. Chu, B. Weigand, V. Vaikuntanathan, "Flow Turbulence Topology in Regular Porous Media: From Macroscopic to Microscopic Scale with Direct Numerical Simulation", Physics of Fluids, 30(6), 065102, 2018, DOI:10.1063/1.5030651

[4] Y. Kuwata, S. Tsuda, K. Suga, "Direct Numerical Simulation of Turbulent Conjugate Heat Transfer in a Porous-Walled Duct Flow", Journal of Fluid Mechanics, 904, A9, 2020, DOI:10.1017/jfm.2020.669

[5] F. Kuwahara, T. Yamane, A. Nakayama, "Large Eddy Simulation of Turbulent Flow in Porous Media", International Communications in Heat and Mass Transfer, 33(4), 411–418, 2006, DOI:10.1016/j.icheatmasstransfer.2005.12.011

[6] R. Deiterding, M. P. Grondeau, "Large eddy simulation of flow over a porous surface with a parallel and adaptive lattice Boltzmann method", In: Proceedings of the Eleventh International Conference on Engineering Computational Technology, Civil-Comp Press, 2025, DOI:10.4203/ccc.2.2.7

[7] W. Sadowski, M. Sayyari, F. di Mare, "Large-Eddy Simulation of a Channel Flow Over an Irregular Porous Matrix", Proceedings in Applied Mathematics and Mechanics, 23, e202300095, 2023, DOI:10.1002/pamm.202300095

[8] S. Succi, "The Lattice Boltzmann Equation for Fluid Dynamics and Beyond", Oxford University Press, Oxford, 2001.

[9] Z. Guo, C. Shu, "Lattice Boltzmann Method and Its Applications in Engineering", World Scientific, Singapore, 2013.

[10] C. Coreixas, B. Chopard, J. Latt, "Comprehensive Comparison of Collision Models in the Lattice Boltzmann Framework: Theoretical Investigations", Physical Review E, 100(3), 033305, 2019, DOI:10.1103/PhysRevE.100.033305

[11] S. Hou, J. Sterling, S. Chen, G. D. Doolen, "A Lattice Boltzmann Subgrid Model for High Reynolds Number Flows", Fields Institute Communications, 6, 1994, DOI:10.48550/arXiv.comp-gas/9401004

[12] M. Grondeau, R. Deiterding, "Direct Prediction of Flow Noise Around Airfoils Using an Adaptive Lattice Boltzmann Method", In B. Stoevesandt, G. Schepers, P. Fuglsang, Y. Sun (Eds.), Handbook of Wind Energy Aerodynamics, Springer, 2021, DOI:10.1007/978-3-030-05455-7_74-1

[13] O. Malaspinas, "Increasing Stability and Accuracy of the Lattice Boltzmann Scheme: Recursivity and Regularization", 2015, DOI:10.48550/arXiv.1505.06900

[14] R. Deiterding, "Block-Structured Adaptive Mesh Refinement – Theory, Implementation and Application", European Series in Applied and Industrial Mathematics: Proceedings, 34, 97–150, 2011,DOI:10.1051/proc/201134002

[15] D. Kashyap, M. P. Grondeau, R. Deiterding, "Scalable Adaptive Lattice Boltzmann–LES Solver for High Reynolds Number Flows in Porous Media", In: Proceedings of the 8th International Conference on Parallel, Distributed, GPU and Cloud Computing for Engineering, Civil-Comp Press, 2025, DOI:10.4203/ccc.12.1.1

[16] H. Chen, O. Filippova, J. Hoch, K. Molvig, R. Shock, C. Teixeira, R. Zhang, "Grid Refinement in Lattice Boltzmann Methods Based on Volumetric Formulation", Physica A, 362, 158–167, 2006, DOI:10.1016/j.physa.2005.09.036

[17] A. Dupuis, B. Chopard, "Theory and Applications of an Alternative Lattice Boltzmann Grid Refinement Algorithm", Physical Review E, 67, 066707, 2003, DOI:10.1103/PhysRevE.67.066707

[18] M. Berger, P. Colella, "Local Adaptive Mesh Refinement for Shock Hydrodynamics", Journal of Computational Physics, 82, 64–84, 1988, DOI:10.1016/0021-9991(89)90035-1

[19] J. Smagorinsky, "General Circulation Experiments with the Primitive Equations", Monthly Weather Review, 91, 99–163, 1963, DOI:10.1175/1520-0493(1963)091$< 0099 : GCEWTP >$2.3.CO;2

[20] O. Malaspinas, P. Sagaut, "Consistent Subgrid Scale Modelling for Lattice Boltzmann Methods", Journal of Fluid Mechanics, 700, 514–542, 2012, DOI:10.1017/jfm.2012.155

[21] K. Suga, Y. Okazaki, Y. Kuwata, "Characteristics of Turbulent Square Duct Flows Over Porous Media", Journal of Fluid Mechanics, 884, A7, 2020, DOI:10.1017/jfm.2019.914